Österlund, Elmeri; Seppänen, Heli; Bespalova, Kristina; Miikkulainen, Ville; Paulasto-Kröckel, Mervi

Atomic layer deposition of AlN using atomic layer annealing - Towards high-quality AlN on vertical sidewalls

Published in:
Journal of Vacuum Science and Technology A: Vacuum, Surfaces and Films

DOI:
10.1116/6.0000724

Published: 01/05/2021

Document Version
Publisher's PDF, also known as Version of record

Please cite the original version:
Österlund, E., Seppänen, H., Bespalova, K., Miikkulainen, V., & Paulasto-Kröckel, M. (2021). Atomic layer deposition of AlN using atomic layer annealing - Towards high-quality AlN on vertical sidewalls. *Journal of Vacuum Science and Technology A: Vacuum, Surfaces and Films*, *39*(3), Article 032403.
https://doi.org/10.1116/6.0000724

JVST A
Journal of Vacuum Science & Technology A

Atomic layer deposition of AlN using atomic layer annealing—Towards high-quality AlN on vertical sidewalls EP

Cite as: J. Vac. Sci. Technol. A **39**, 032403 (2021); https://doi.org/10.1116/6.0000724
Submitted: 16 October 2020 . Accepted: 16 February 2021 . Published Online: 08 March 2021

Elmeri Österlund, Heli Seppänen, Kristina Bespalova, Ville Miikkulainen, and Mervi Paulasto-Kröckel

COLLECTIONS

Paper published as part of the special topic on Atomic Layer Deposition (ALD)

EP This paper was selected as an Editor's Pick

View Online
Export Citation
CrossMark

ARTICLES YOU MAY BE INTERESTED IN

Atomic layer deposition of sodium fluoride thin films
Journal of Vacuum Science & Technology A **39**, 032405 (2021); https://doi.org/10.1116/6.0000847

Thermal atomic layer etching: A review
Journal of Vacuum Science & Technology A **39**, 030801 (2021); https://doi.org/10.1116/6.0000894

Phosphites as precursors in atomic layer deposition thin film synthesis
Journal of Vacuum Science & Technology A **39**, 032404 (2021); https://doi.org/10.1116/6.0000844

JVST A
Journal of Vacuum Science & Technology A

ARTICLE

avs.scitation.org/journal/jva

Atomic layer deposition of AlN using atomic layer annealing—Towards high-quality AlN on vertical sidewalls

Cite as: J. Vac. Sci. Technol. A **39**, 032403 (2021); doi: 10.1116/6.0000724
Submitted: 16 October 2020 · Accepted: 16 February 2021 ·
Published Online: 8 March 2021

View Online Export Citation CrossMark

Elmeri Österlund,[1,a)] Heli Seppänen,[2] Kristina Bespalova,[1] Ville Miikkulainen,[3]
and Mervi Paulasto-Kröckel[1]

AFFILIATIONS

[1] Department of Electrical Engineering and Automation, Aalto University, PO Box 13500, 00076 Aalto, Finland
[2] Department of Electronics and Nanoengineering, Aalto University, PO Box 13500, FI-00076 Aalto, Finland
[3] Department of Chemistry and Materials Science, Aalto University, P.O. Box 16100, FI-00076 Aalto, Finland

Note: This paper is part of the 2021 Special Topic Collection on Atomic Layer Deposition (ALD).
[a)] **Present address:** Kyocera Tikitin Oy, Tietotie 3, 02150, Espoo, Finland; **electronic mail:** elmeri.osterlund@aalto.fi

ABSTRACT

Atomic layer deposition (ALD) of aluminum nitride (AlN) using in situ atomic layer annealing (ALA) is studied for microelectromechanical systems (MEMS). Effective piezoelectric in-plane actuation and sensing requires deposition of high crystal quality and (0002) oriented AlN on vertical sidewalls of MEMS structures. Previous studies have shown that the crystal quality of ALD AlN can be significantly improved using ALA but have not studied the conformal coverage or crystal quality on metal electrodes, which are required for piezoelectric MEMS devices. In this study, AlN thin films are deposited on Si, Al, Pt, and on vertical sidewalls etched into Si. The AlN microstructure and properties are studied using x-ray diffraction methods, transmission electron microscopy, and Fourier transform infrared spectroscopy. The conformal coverage is evaluated by measuring the film thickness on the vertical sidewalls. The effects of postdeposition annealing are studied as well. This study aims to enable effective piezoelectric actuation and sensing for MEMS sensors. The conformal coverage of the ALA ALD process is excellent and AlN has the best crystal quality and degree of orientation when deposited on Al. The as-deposited films contain oxygen impurities, which might be detrimental to the piezoelectric properties of AlN. Annealing at high temperatures reduced the number of impurities but did not improve the crystal quality.

I. INTRODUCTION

Piezoelectric aluminum nitride (AlN) thin films are used in many microelectromechanical systems (MEMS), such as thin film bulk acoustic resonators,[1,2] microphones,[3] and piezoelectric micromachined ultrasound transducers.[4,5] Piezoelectric actuation and sensing provide many advantages over electrostatic methods such as higher electromechanical coupling and lower power consumption.[6] AlN is a suitable material for piezoelectric MEMS due to its low dielectric permittivity ($\varepsilon_{33} = 10.5$) and relatively high transverse piezoelectric coefficient ($e_{31,f} = -1.05\ \mathrm{C/m^2}$), resulting in competitive figures of merit for actuation and sensing.[7] Furthermore, AlN thin films are mechanically strong,[8] chemically stable,[9] and compatible with common manufacturing processes and materials.

Piezoelectric AlN is most commonly deposited using reactive sputtering, which offers fast deposition rates and good crystal quality. However, sputtering suffers from poor conformal coverage and the AlN crystal structure is tilted on vertical structures. The [0001] or *c*-axis of AlN is tilted with respect to the surface normal when sputtered on vertical sidewalls.[10] For optimum electromechanical coupling, the *c*-axis of AlN should always be parallel with the local surface normal. The deposition of *c*-axis oriented AlN on vertical sidewalls is required for novel piezoelectric in-plane actuation and sensing, as illustrated in Fig. 1, which could improve the performance of inertial MEMS sensors, such as three-axis gyroscopes. Furthermore, the deposition of conformal piezoelectric AlN can be used in the fabrication of new three-dimensional electromechanical metamaterials,[11] and MEMS resonators with

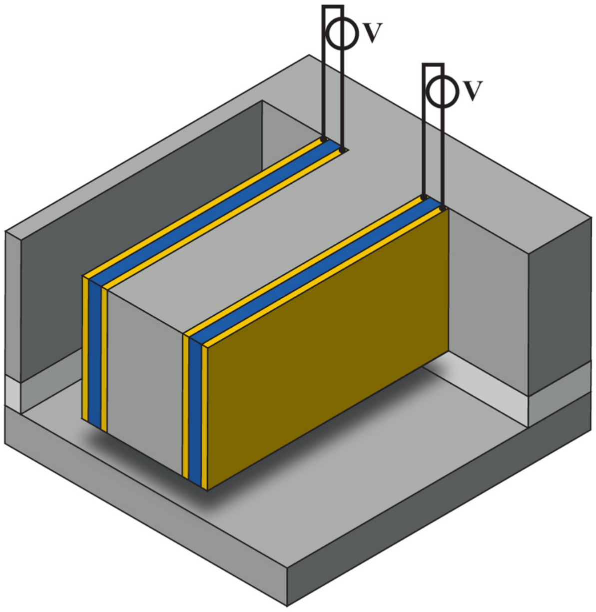

FIG. 1. Schematic of a piezoelectric sidewall structure for in-plane actuation and sensing. AlN is on the vertical sidewalls of an Si beam along with top and bottom electrodes. In actuation, applied voltage over the piezoelectric AlN layer generates in-plane movement by deflecting the beam, and in sensing the in-plane movement of the structure generates an electrical charge.

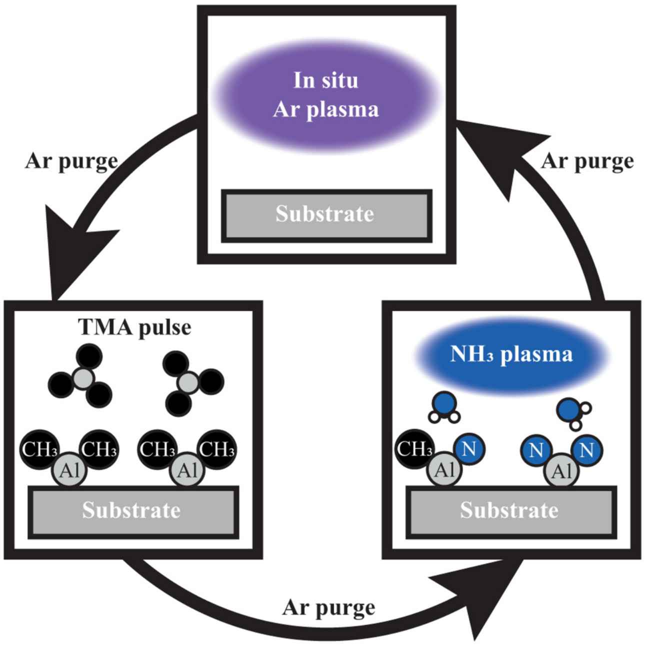

FIG. 2. Steps of the ALA ALD process cycle: Ar ALA treatment, TMA pulse, and NH_3 plasma pulse.

lithographically defined multiple resonance frequencies on the same chip.

Chemical vapor deposition (CVD) generally has better conformal coverage[12] and metal-organic CVD (MOCVD) has been used to grow high-quality AlN on vertical sidewalls.[13] However, MOCVD requires growth temperatures above 1000 °C for high crystal quality AlN (Ref. 13) and results in residual stresses of more than 1.5 GPa,[8] both of which are a challenge for process integration. Atomic layer deposition (ALD), on the other hand, uses lower growth temperatures while being known for unparalleled conformal coverage. Furthermore, ALD offers excellent process control for film thickness, uniformity, and residual stresses. Previously, the crystal quality of ALD AlN films has not been adequate for piezoelectric applications because the films have been polycrystalline without preferential (0002) orientation or nearly amorphous.[14,15] Although recently, the piezoelectric properties of plasma-enhanced ALD (PEALD) AlN on Ni(111) have been demonstrated successfully.[16] The crystal quality of PEALD AlN has been significantly improved using in situ atomic layer annealing (ALA),[17] where an additional plasma annealing step is added to the ALD cycle. Using ALA, (0002) textured AlN thin films were deposited on (0001) sapphire, a well-suited substrate for AlN deposition. However, for piezoelectric applications, AlN needs to be deposited on conductive material so that an electric field can be applied over the film. Moreover, sapphire is not commonly used in MEMS technologies. Previous experiments also show that the crystal quality of AlN deposited on Si(100) is improved using ALA.[18]

In this study, AlN thin films are deposited on bare and metalized Si substrates using ALA PEALD. The microstructure and crystal quality of the films are studied using x-ray diffraction (XRD), transmission electron microscopy (TEM), Fourier transform infrared spectroscopy (FTIR), and atomic force microscopy (AFM). The residual stresses are measured from wafer curvature and compared to stresses derived from the XRD results. The piezoelectric properties are studied by fabricating 72 mm long cantilevers and measuring the tip deflection as a function of an applied voltage. The conformality of the ALD process is studied by depositing AlN on the vertical sidewalls of 100 μm deep and wide etched trenches. Finally, AlN films are annealed to study the thermal stability of the films and whether the crystal quality can be improved after deposition.

II. METHODS

A. Atomic layer deposition

The AlN films were deposited in a Beneq TFS 500 13.56 MHz capacitively coupled plasma reactor. The precursors for the films were trimethylaluminum [$Al_2(CH_3)_6$, TMA, >99.5% pure, Volatec] and ammonia (NH_3, 99.9999% pure, AGA) and the reactor temperature was 300 °C. The three-step ALD cycle is presented in Fig. 2, with an added Ar (99.9999% pure) plasma annealing step. 1000 cycles were used to grow the AlN films.

The deposition process starts with the Ar ALA step to first clean the substrate surface and to anneal the AlN monolayers during subsequent cycles. The Ar plasma power is 200 W and the plasma is on for 20 s, resulting in a sample bias of approximately 5 V. After the plasma annealing, a 0.3 s TMA pulse is introduced into the reactor. The final step in the cycle is a 15 s and 200 W NH_3 plasma pulse. The reactor pressure is approximately 10 mbar during the deposition. The reactor is purged with Ar between steps and Ar is also used as the carrier gas. The purge times were 4, 6, and 0.1 s after TMA, NH_3, and ALA, respectively. This ALD process was developed in previous studies and results in self-limited growth.[18,19] The base pressure of the reactor without any gas flows is 0.7 mbar.

B. Substrates

Four different types of substrate-film stacks were used for AlN deposition. The first two types were bare Si (I) and Al on Si (II). The latter two used a thin AlN diffusion barrier between the Si wafer and Al (III) or Pt/Cr (IV) electrode. The AlN diffusion barriers were deposited using the same ALD process as the main AlN film. A second purpose of the AlN diffusion barrier is to promote the growth of the electrode into a structure and orientation that would, in turn, promote the growth of AlN. All the substrate types are illustrated in Fig. 3. 300 ALD cycles were used for the diffusion barriers instead of 1000 cycles used for the main AlN layers.

The Si substrates used were 100 mm diameter wafers with (111) oriented surfaces and were p-type boron-doped with a resistivity of 10–20 Ω cm and a thickness of 525 $\pm$ 25 μm. The wafers were off-cut so that the angle between the surface normal and Si [111] was 4° $\pm$ 1°.

The Al and Pt metal layers were deposited using DC sputtering in an Oxford Instruments Plasmalab 400. The Al layers were deposited using an Ar flow of 50 sccm and a DC power of 2000 W at a chamber pressure of 0.5 Pa (3.8 mTorr) and a chuck temperature of 37 °C. The Pt layer was deposited using an Ar flow of 70 sccm, a DC power of 500 W at 0.7 Pa (4.9 mTorr), and 37 °C. A Cr layer was used underneath Pt to improve adhesion and it was sputtered using an Ar flow of 50 sccm, 200 W DC power at 0.5 Pa (3.8 mTorr), and 37 °C.

C. Film characterization

The thickness and refractive index of the AlN films were mapped using spectroscopic ellipsometry over a wavelength range of 190–2500 nm in a Semilab SE-2000 ellipsometer. The residual stress was analyzed by measuring the curvature of the substrate before and after AlN deposition in a Toho Technology FLX 2320-S. The curvature was measured in two perpendicular directions over the substrates. The sheet resistances of the films were mapped in an Advanced Instrument Technology CMT-SR2000N four-point probe station.

The microstructure and crystal quality of the AlN films were studied with XRD in a Rigaku SmartLab diffractometer using CuK_α radiation with wavelengths of 1.540 593 Å (α1) and 1.544 414 Å (α2). The diffractometer was operated in three different optical configurations, high-resolution (HRXRD), in-plane, and diffraction mapping. TEM and FTIR were used to complement the XRD characterization. The crystal quality was characterized using HRXRD 2θ–ω diffractograms and ω x-ray rocking curves (XRCs) of the AlN0002 reflection. The HRXRD configuration used a parallel beam, Ge(220)×2 monochromator, and a 5° soller slit on both the incident and diffracted beam path. The 2θ axis of the diffractometer was calibrated using an Si powder reference sample.

In-plane XRD can measure the in-plane *hki*0 reflections of (0002) oriented AlN and their rocking curves[20] and was used to further study the AlN films. $2\theta_\chi$–ϕ diffractograms and ϕ curves, analogous to 2θ–ω diffractograms and ω curves, respectively, were measured using a parallel beam with a 0.5° in-plane parallel slit collimator and analyzer on the incident and diffracted beam path, respectively.

The diffraction maps were recorded using a focused beam and an open 2D detector at varying angles of sample χ tilt. The resulting χ–2θ diffraction maps were used to study the texture of the films and show if the symmetrical reflections are tilted about the surface normal and the distribution of the tilting. The different diffractometer and sample angles are illustrated in Fig. 4. The XRD results were fitted using a pseudo-Voigt function in a least squares sense to accurately determine the location and full widths at half maximum (FWHM) of the reflections.

TEM imaging was used to study the AlN microstructure as well. First, focused ion beam (FIB, JEOL JIB-4700F) milling and

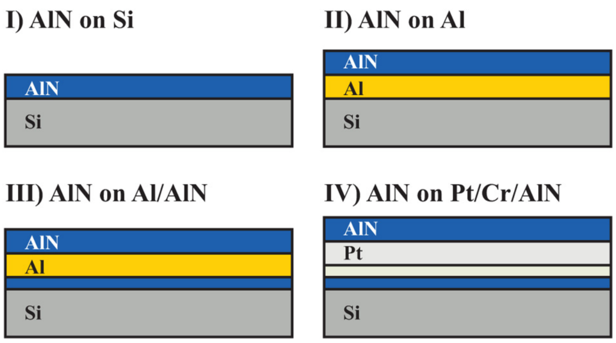

FIG. 3. Four types of substrate-film stacks used in this study for AlN deposition.

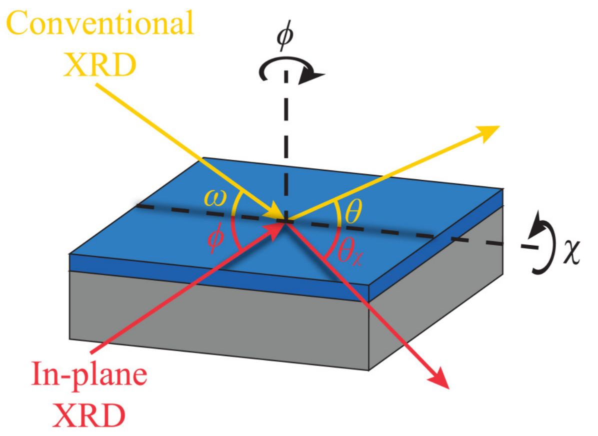

FIG. 4. Diffractometer and sample angles in conventional and in-plane XRD.

polishing with Ga ions were used to make an approximately 100 nm thick cross section of the AlN film. A high-resolution JEOL JEM-2800 microscope using an acceleration voltage of 200 kV was used to image the cross section using high-resolution (HRTEM), bright-field, and scanning TEM (STEM) modes.

The FTIR absorbance spectra of AlN on Si (I) were measured using a Bruker ALPHA II spectrometer in transmission mode from 400 to 4000 cm^{-1} at a resolution of 4 cm^{-1} and normal incidence. The effect of the Si substrate was removed from the measurements. The AlN absorption lines were fitted using a Lorentzian distribution.

The film surface morphology was studied using AFM in a Bruker Dimension Icon microscope. AFM micrographs were measured over a $5 \times 5\,\mu\mathrm{m}^2$ area using an Si cantilever, with a nominal tip radius of 7 nm in tapping mode.

The piezoelectric properties of the films were characterized by measuring the $e_{31,f}$ coefficient by measuring the deflection of 5 mm wide and 72 mm long fabricated cantilevers as a function of applied voltage over the AlN layer.[21] The measurements were performed using a Radiant Technologies Precision LC II system in combination with a cantilever test fixture and a fiber optic displacement sensor. The voltage-deflection curves were fitted in a least squares sense using the equation

$$e_{31,f} = -\frac{1}{3}\frac{Et_c^2}{(1-\nu)c_f x_1(2x_2 - x_1)}\frac{z(x_2)}{V}, \tag{1}$$

where E is Young's modulus, t_c is the thickness, ν is Poisson's ratio of the cantilever, c_f is the ratio of the top electrode to cantilever width, x_1 is the length of the top electrode from the test fixture clamp and x_2 is the distance between the displacement sensor and the clamp, $z(x_2)$ is the deflection of the cantilever, and V is the applied voltage.[21] Sputtered Al was used as the top electrode. The fabricated cantilevers had a nominal unclamped length of 39 mm and a electrode width of 0.1 or 1.0 mm.

D. Postdeposition annealing

Samples from wafers with AlN on Si (type I) and Al (type II) were annealed after deposition in a Webb RD-M vacuum furnace to study the effect of annealing on AlN crystal quality and how the films would withstand further processing. The samples were annealed at temperatures between 300 and 1000 °C for 10 h. The base pressure in the furnace was less than 0.1 mPa, and the heating rate was 15 °C/min. After annealing, the films were remeasured using XRD, FTIR, and AFM.

E. Conformal coverage

The conformal coverage of the ALD process was studied by using patterned Si substrates. 100 μm deep and 100 μm wide trenches were etched into 200 μm thick Si(110) substrates using a previously developed potassium hydroxide wet etching process,[13] which results in smooth and vertical sidewalls with Si(111) surfaces. The thickness of the AlN film on the sidewalls was measured by first cleaving samples perpendicular to the sidewalls and then imaging the formed cross section using scanning electron microscopy (SEM, Zeiss Supra 40) along the depth of the sidewall at 10 μm intervals.

III. RESULTS AND DISCUSSION

The average thickness of the AlN layers on Si and Al after 1000 ALD cycles is 118.8 nm with a standard deviation of 1.33 nm and a uniformity of 2.51%. The measured refractive index is 1.98(3) at a wavelength of 632.8 nm. The average thickness of the diffusion barriers is 34.0(1.6) nm. The growth per cycle (GPC) is then 1.2 Å on average. The GPC and refractive index seem to depend slightly on the history of the reactor. During consecutive AlN depositions, the GPC decreases, while the refractive index increases. This could be a result of the improving nitridization and reduction of residual oxygen in the reactor. Al is more reactive with O than N [Gibb's free energy $\Delta G(\mathrm{Al_2O_3}) = -1480$ kJ/mol vs $\Delta G(\mathrm{AlN}) = -253$ kJ/mol (Ref. 22)] and $\mathrm{Al_2O_3}$ formed within the AlN film could lead to a lower refractive index due to the lower index of AlO.[23] Another possibility is the formation of Al-N-O oxynitrides.

Directly on Si, the sheet resistance of the AlN layer is more than 16 $\mathrm{M}\Omega/\square$ (more than the nominal measuring range). The sheet resistance of the blank wafer was 411 $\Omega/\square$. It was not possible to measure the sheet resistance of AlN on metal layers, because the sheet resistance mapping tool pushed the probes through the AlN film into the metal.

The surfaces of AlN films on Si and Al are relatively smooth with root-mean-square surface roughnesses of 1.8 and 1.7 nm for AlN on Si and Al, respectively. However, AlN on Si (I) seems to have an ultrafine grain structure with small, round, and uniform grains with a mean size of approximately 31 nm. Whereas AlN on Al, the mean grain size seems significantly larger, approximately 70 nm, and the shape of the grains is markedly different. Instead of round, the grains are oval-shaped with wider and deeper gaps between them. See supplementary material[54] for AFM micrographs of both AlN surfaces.

The conformal coverage on the vertical sidewalls is excellent. Despite the directionality added by the plasma steps, the ALA PEALD process retains the excellent conformal coverage of ALD and the coverage is significantly better than previously obtained using MOCVD, where the film thickness decreased from approximately 140 to 40 nm down a 100 μm deep trench.[13] The average thickness of the AlN film is 124 nm with a standard deviation of 14 nm and the film thickness does not decrease significantly down the sidewall, as can be seen in Fig. 5(a). On the contrary, the film thickness is approximately 115 nm at the top of the trench and increases to a maximum of 152 nm at a trench depth of 30 μm and then settles back to approximately 110 nm at the trench bottom, where the trench width is only 2.9 μm, instead of 100 μm, as shown in Fig. 5(b).

The film on the vertical sidewall is thicker on average than on the planar substrates, and the deviation is higher as well. The differences are at least in part caused by the different measurement methods. The film thickness on planar substrates can be measured more accurately using ellipsometry compared to measuring the thickness from cross-sectional SEM micrographs. However, it is unlikely that the change in the measured film thickness down the sidewall is caused only by the measurement error and similar

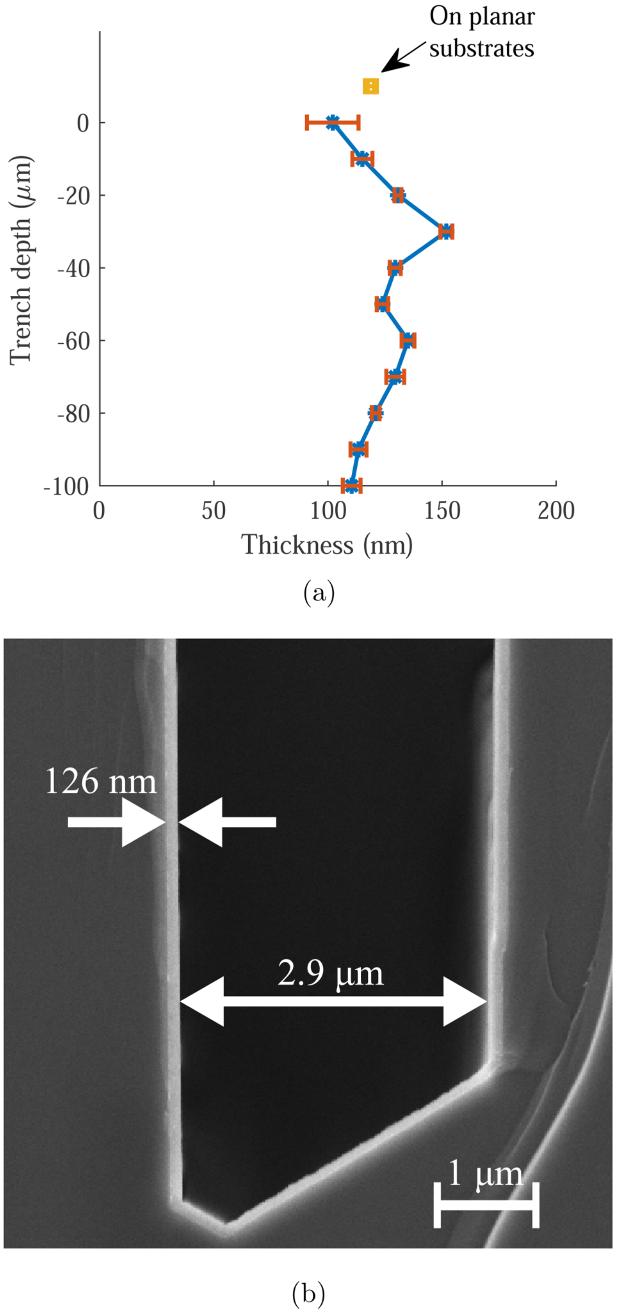

(a)

(b)

FIG. 5. Thickness and cross-sectional SEM micrographs of AlN deposited on vertical sidewalls. (a) Thickness of the AlN film down the vertical sidewall. (b) AlN film at the bottom of the trench.

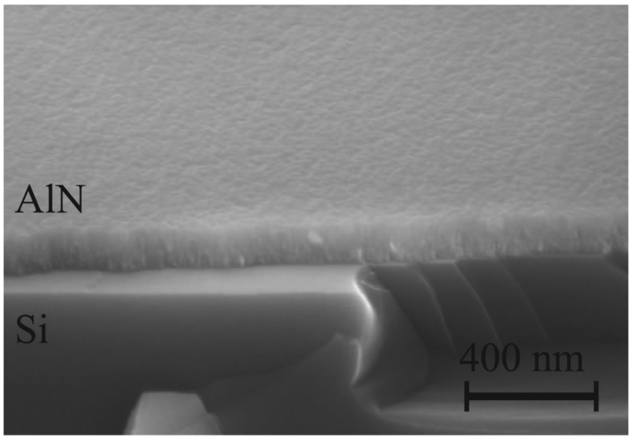

FIG. 6. Cleaved AlN film on the vertical sidewall, showing the crystalline microstructure of the film, at a trench depth of 50 μm.

thickness profiles are observed in the MOCVD AlN films as well.[13] The uneven growth rates down the sidewall can be due to insufficient purge times causing precursors to linger in the trench and leading to a more CVD like growth. Another possibility is that AlN grows faster on the rougher etched surface due to the availability of terraces and other nucleation sites.

In-plane XRD measurements show that the AlN films on the vertical sidewalls are crystalline, but seem to lack the desired *c*-axis orientation. SEM micrographs of cleaved cross sections show that the films are crystalline and seem to have columnar structure, typical of *c*-axis oriented AlN films, as shown in Fig. 6.

The χ–2θ diffraction maps of AlN on substrate types I–IV are presented in Fig. 7. The AlN0002 reflection is present for all the films and its intensity and width indicate that AlN is most crystalline when grown on Al (type II). The Al and Pt layers sputtered on the AlN diffusion barrier (types III and IV) are polycrystalline, with a weak preferential (111) orientation. The Al layer directly on Si (type II) is strongly (111) textured. The off-cut of the Si substrate is visible in the diffraction maps as a shift of the Si111 maximum to a χ angle of 4°, and interestingly, for AlN on Al (II) in Fig. 7(b), both Al[111] and AlN[0002] have similar tilts with maximums at χ angles of 4° and 3°, respectively. On other types of substrates, the maximum of the very wide AlN0002 reflection is centered around a χ angle of 0°. The polycrystalline Pt111 reflection in Fig. 7(d) is centered around $\chi = 0°$ as well, while the polycrystalline Al111 in Fig. 7(c) has two maximums at approximately $-5°$ and 6°.

Table I presents the HRXRD results for the location and width of the AlN0002 reflections and the location and width of its rocking curve, given by the pseudo-Voigt fit. The lattice constant *c* is calculated from the location of 0002 reflection. The intensity of the 0002 reflection of AlN on Pt/Cr/AlN (type IV) was too weak to be measured using HRXRD and is not shown. The measured ω XRCs are presented in Fig. 8 and show that AlN on Al (II) has preferential 0002 or *c*-axis texture. The measured FWHM of 6.58° indicates that the deposited layer is not as well oriented as typical MOCVD or sputtered AlN thin films. Typical values for MOCVD films of a similar thickness are 1.2° (Ref. 13) and for 1–2 μm thick sputtered films typical values are in the range of 1.2°–2°.[24] AlN deposited on other types of substrates has only very weak texturing

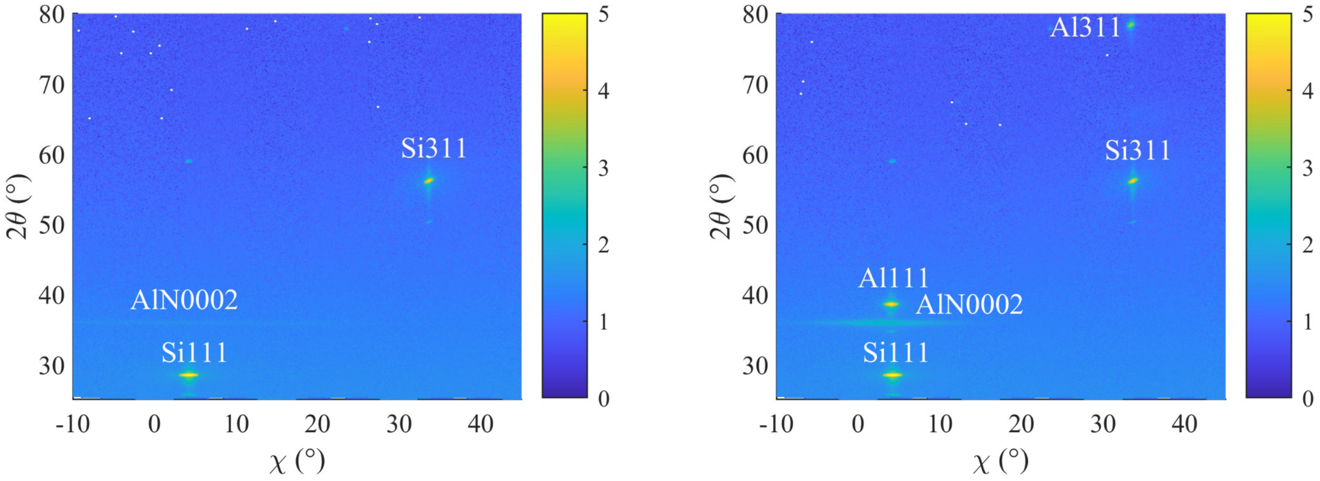

(a) AlN on Si (I).

(b) AlN on Al (II).

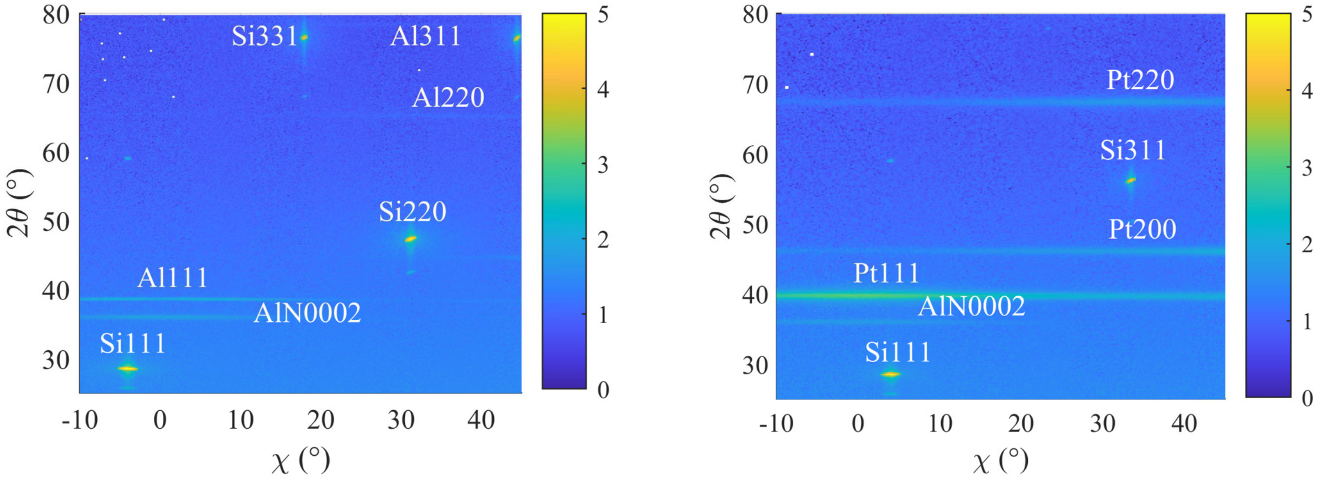

(c) AlN on Al/AlN (III).

(d) AlN on Pt/Cr/AlN (IV).

FIG. 7. Measured χ–2θ XRD maps of AlN films on substrates I–IV. The reflected intensity in arbitary units (a.u.) is plotted using a logarithmic scale for visualization purposes. (a) AlN on Si (I). (b) AlN on Al (II). (c) AlN on Al/AlN (III). (d) AlN on Pt/Cr/AlN (IV).

TABLE I. HRXRD results for the location and FWHM of the AlN0002 reflection, along with the calculated lattice constant *c*, and the location and FWHM of its rocking curve.

Film	2θ–ω			XRC	
	2θ (deg)	FWHM (deg)	*c* (Å)	ω (deg)	FWHM (deg)
I	35.94	0.48	4.99	10.27	29.42
II	35.94	0.42	4.99	17.56	6.58
III	35.94	0.44	4.99	15.76	19.12

or no preferential orientation at all. For AlN on Al/AlN and Pt/AlN, the 30 nm AlN diffusion barrier contributes to the XRD results as well. In the HRXRD measurements, the goniometer was aligned to the AlN0002 reflection. The calibration using an Si powder reference sample resulted in a 0.03° error in 2θ around 36° based on the measured and reference reflections for Si and this has been taken into account in the results. See supplementary material[54] for the measured HRXRD 2θ–ω diffractograms.

The *hki*0 type reflections of AlN were measured using in-plane XRD, and the results are summarized in Table II for

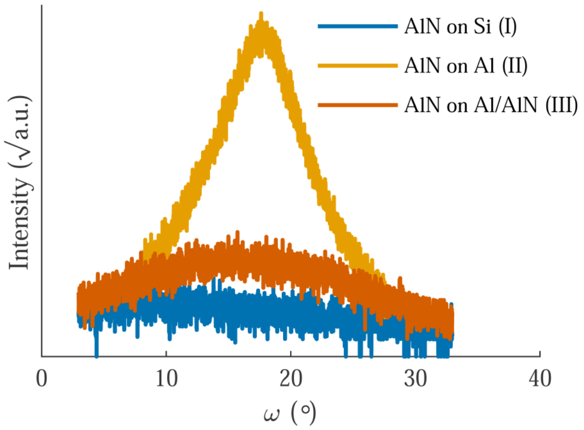

FIG. 8. XRCs of the AlN0002 reflection. The square root of reflected intensity is used for visualization purposes.

substrate types I and II. The lattice constant a is calculated and averaged from the locations of the measured $hki0$ reflections. For AlN on Al (II), ϕ XRCs were measurable for reflections $10i0$, $11i0$, and $20i0$, with an average FWHM of 8.45(15)°. Furthermore, these reflections had six poles, indicating an in-plane orientation and mosaic texture of the AlN crystallites. The orientational relationship to Al is AlN(0002)||Al(111) and AlN[$11i0$]||Al[110], which has been previously observed as well.[25] None of the other films had measurable rocking curves or poles, indicating a lack of in-plane orientation. See supplementary material[54] for the measured $10i0$ and $11i0$ in-plane diffractograms. The angles of incidence ω in the in-plane XRD measurements were 0.19°–0.20° and 0.24°–0.25° for AlN on Si (I) and Al (II), respectively.

Cross-sectional TEM micrographs of AlN on Pt (IV) show that the AlN films contain both highly (0002) and randomly oriented grains. A grain with preferential (0002) orientation is shown in Fig. 9(a), while a randomly oriented one is shown in Fig. 9(b). Figure 9(c) presents a dark-field STEM micrograph, which shows the AlN grains with preferentially and randomly oriented microstructures as bright and dark grains, respectively. The majority of the AlN grains are randomly oriented. The differences in measured crystallinity in XRD are likely caused by different amounts of preferentially and randomly oriented grains in each film.

TABLE II. Results of in-plane XRD measurements on AlN films on Si (I) and Al (II) for the location and FWHM of $10i0$ and $11i0$ reflections. The lattice constant a is the average of all measured reflections.

Film	$10i0$		$11i0$		
	$2\theta_\chi$ (deg)	FWHM (deg)	$2\theta_\chi$ (deg)	FWHM (deg)	a (Å)
I	33.36	1.75	59.31	1.90	3.109(11)
II	33.20	1.82	59.22	2.04	3.119(3)

The best crystallinity is achieved on Al out of the three substrate materials, likely because the in-plane lattice mismatch between AlN and Al is the smallest. The lattice mismatches between AlN and Al(111), Pt(111), or Si(111) are −8.65%, −12.16%, and 18.98%, respectively. In addition to a small lattice mismatch, the growth of (0002) oriented AlN requires that the underlying material is well oriented, as evidenced by the difference in AlN crystal quality on the two different Al layers. Differently oriented crystallites of the substrate will of course have different in-plane lattice constants. Another explanation for the differently oriented AlN crystallites could be local surface roughness.[24] However, it does not seem to be the case here based on the TEM results.

The lattice mismatch of $Al_2O_3(0001)$ substrates to AlN is 13.29%.[26] However, an FWHM of 0.04° for the 0002 XRC of ALD AlN on $Al_2O_3(0001)$ has been achieved, despite the relatively large mismatch.[17] The smaller FWHM (0.04° vs 6.58°) means that the preferential (0002) orientation of AlN crystallites is significantly better than the orientation of AlN on Al in this study. Thus, there must be other contributing factors to the crystal structure other than the lattice mismatch. One clear difference is the plasma power used in the ALA step (300 vs 200 W). The 200 W used in this study was the maximum available power from the equipment. Another contributing factor might be the concentration of impurity atoms incorporated into the AlN films.

The piezoelectric testing of the cantilevers showed that all the AlN films contained defects that lowered the effective dielectric strength of the films. Most of the samples failed at applied voltages below 2 V, which was not enough to generate measurable displacement of the cantilever tip to measure the $e_{31,f}$. One sample of AlN on Al withstood 30 V of voltage and generated a displacement of 19 nm, corresponding to an $e_{31,f}$ of $-0.38\ \mathrm{C/m^2}$. This measurement agrees very well with the previous results for the piezoelectric properties of PEALD AlN.[16] However, it is significantly lower than the full $e_{31,f}$ of $-1.05\ \mathrm{C/m^2}$ for thin film AlN.[6] No clear reason for the low dielectric strength, such as pinholes or other defects, was discovered in TEM results.

The piezoelectric properties of AlN seem to depend on the FWHM of the 0002 XRC.[27–31] Piezoelectric properties have been measured for AlN films with rocking curve FWHM as high as 10° (Ref. 30) and once the FWHM is less than 2°, AlN should reach its full piezoelectric properties. For the converse piezoelectric effect, the crystal quality requirements might be even less strict.[32] Based on the AlN0002 XRC widths (Table I), only the AlN film on Al with an FWHM of 6.58° can be piezoelectric, while the rest of the films are not crystalline enough for the emergence of piezoelectric properties. While AlN on Al is piezoelectric ($e_{31,f} = -0.38\ \mathrm{C/m^2}$), it is likely not enough for practical MEMS devices and the crystallinity should be improved further.

The AlN films were annealed after deposition to see if the crystal quality could be improved and how the films would withstand further processing. Using FTIR and XRD, the effects of annealing on film impurities, crystal quality, and residual stresses were studied. Only the AlN films on Si (I) and on Al (II) were annealed because on Si high annealing temperatures can be potentially reached without melting or high thermal stresses, and on Al the AlN crystallinity is the most promising. AlN on Al films were

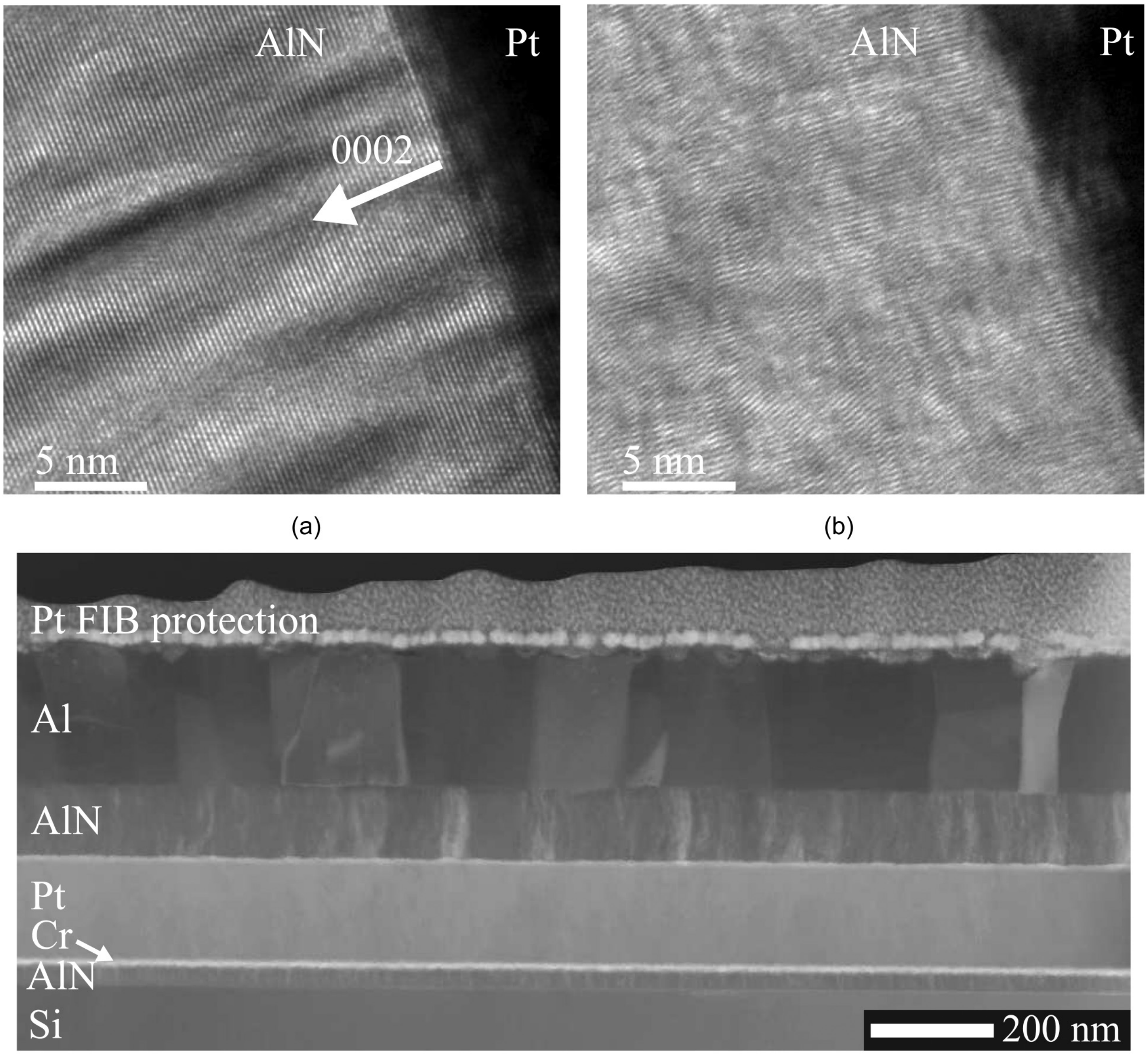

(a)

(b)

(c)

FIG. 9. TEM micrographs of AlN on Pt/Cr/AlN (type IV). (a) HRTEM micrograph of an AlN grain with preferential (0002) orientation. (b) HRTEM micrograph of AlN with randomly oriented polycrystalline microstructure. (c) An annular dark-field STEM micrograph of AlN on Pt with Al top electrode.

not annealed beyond 600 °C because the melting point of Al is 660 °C. Moreover, at lower annealing temperatures of 300 and 400 °C, the films developed fractures and after annealing at 600 °C the films fracture completely.

The FTIR absorption spectra for the as-deposited and annealed AlN films on Si are presented in Fig. 10. In addition to a strong AlN absorption line at around 670 cm^{-1}, additional absorption lines are observed. The line at 460 cm^{-1} corresponds to Al-O (Ref. 33) and indicates that O atoms have been incorporated into the film and reacted with Al. The lines around 1560 and 3200 cm^{-1} indicate the presence of NH_2, both on the surface of the film and within the film itself.[34] The lines around 1500 and 2200 cm^{-1} correspond to various C-H_x bending modes[35,36] and N triple bond stretching in an Al-N_2 complex,[37,38] respectively.[15] The broad line around 3600 cm^{-1} is likely due to AlOH surface species,[39] which are present in the AlOOH surface oxide of AlN.[40]

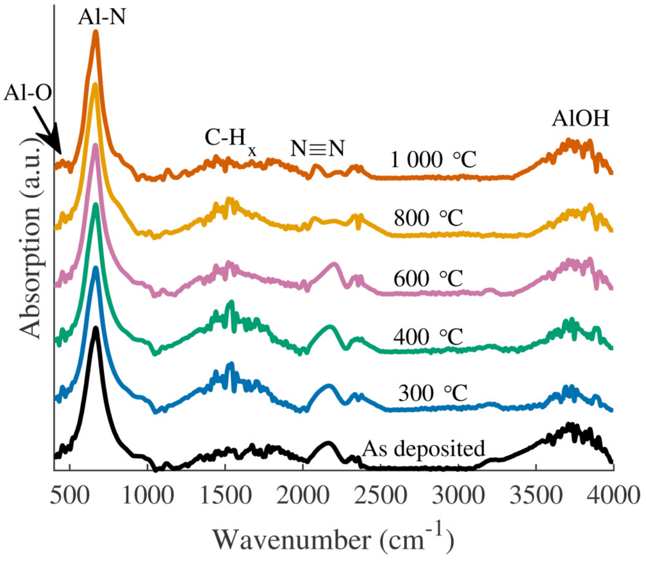

FIG. 10. Measured FTIR absorption spectra for as-deposited and annealed AlN films on Si (I) from 400 to 4000 cm^{-1}. The square root of intensity is used for visualization purposes.

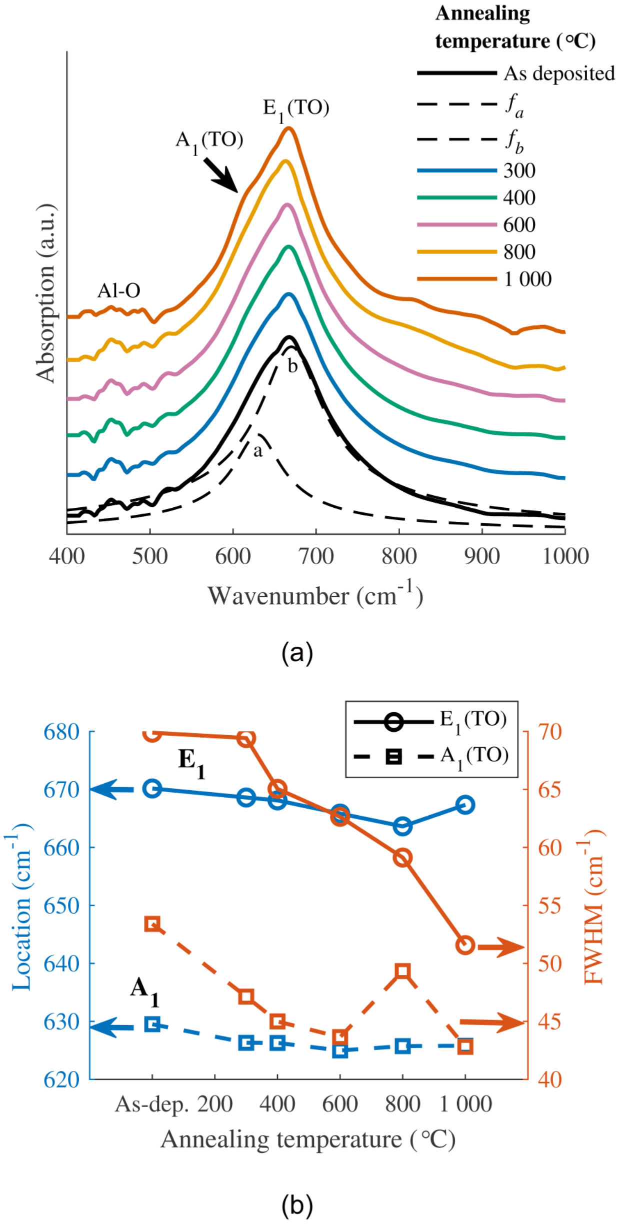

(a)

(b)

FIG. 11. The AlN E$_1$(TO) and A$_1$(TO) FTIR results of as-deposited and annealed AlN films on Si (I). Two Lorentzian distributions [(a) and (b)] were used to fit the measured absorption line of AlN and they are shown as dashed lines for the as-deposited film as an example. (a) The FTIR absorption spectra around the AlN E$_1$(TO) absorption mode. The square root of intensity is used for visualization purposes. (b) Measured location and FWHM of the AlN E$_1$(TO) and A$_1$(TO) lines as a function of annealing temperature.

Previously published results on PEALD of AlN have detected N, H, C, and O impurity atoms using time-of-flight elastic recoil detection analysis (ToF-ERDA) within the bulk of the film.[15,19,36,41,42] These impurities have also resulted in similar FTIR spectra as observed here.[15,36]

The changes in the FTIR spectra as a result of postdeposition annealing under vacuum indicate that the concentration of impurities decreases, which is seen as a decrease in the intensity of the absorption lines in Fig. 10. The amount of Al-N$_2$ complexes starts to decrease when AlN is annealed at 800 °C, and the amount of C-H groups decreases when AlN is annealed at 1000 °C. The absorption line due to Al$_2$O$_3$ also reduces in intensity after annealing at 1000 °C.

The AlN absorption lines, shown in more detail in Fig. 11(a), seem to consist of two overlapping lines, and two Lorentzian distributions were required to explain the results. The two distributions are shown in Fig. 11(a) as two dashed lines labeled f_a and f_b for the as-deposited film as an example. The second line (b) at a higher wavenumber is the E$_1$ transverse optical (TO) phonon mode for AlN, which corresponds to crystallites with their [0001] axes perpendicular to the sample surface, in the normal incidence condition, and corresponds to preferentially (0002) oriented AlN. The first line (a) is most likely the A$_1$(TO) phonon mode, which is caused by crystallites with [0001] axes parallel to the sample surface instead. Figure 11(b) presents the location and FWHM of the two lines as a function of annealing temperature.

The estimated stresses using wafer curvature, FTIR, HRXRD, and in-plane XRD are summarized in Table III for the as-deposited and annealed films. Biaxial residual stress can be estimated from the shifts of the measured E$_1$(TO) and A$_1$(TO) from the reference values. The effects of stress are approximately 8 (Ref. 43) and 4 cm^{-1}/GPa (Ref. 44) on E$_1$(TO) and A$_1$(TO), respectively. From the XRD measurements, the biaxial residual stress $\sigma_{\|}$ can be estimated by comparing the measured lattice constants to unstrained

TABLE III. Residual stresses of AlN films on Si (I) and Al (II) estimated using wafer curvature (WC), shifts of E_1(TO) and A_1(TO), and measured lattice constants *c* and *a*.

Temp.	Stress of AlN on Si (I) (GPa)					on Al (II) (GPa)		
(°C)	WC	E_1(TO)	A_1(TO)	*c*	*a*	WC	*c*	*a*
As-dep.	0.433	0.36	3.97	−1.62	−0.25	1.56	−1.68	0.72
300		0.55	3.19	−1.55			−1.96	
400		0.61	3.18	−1.26			−1.80	0.65
600		0.9	2.86	−0.12			−2.16	
800		1.17	3.04	2.44	0.54			
1000		0.71	3.07	1.38	−0.23			

reference values. Using the lattice constant *c* measured with HRXRD, the residual stress is

$$\sigma_{\parallel} = \frac{E}{-2\nu}\varepsilon_c = \frac{E}{-2\nu}\frac{c - c_0}{c_0}, \tag{2}$$

where *E* is Young's modulus, ν is Poisson's ratio, ε_c is the out-of-plane strain, and c_0 is the unstrained reference.[45] A reference value of 4.980 79 Å (Ref. 46) was used for c_0. Similarly, the residual stress can be calculated from the lattice constant *a* measured with in-plane XRD as

$$\sigma_{\parallel} = \frac{E}{1-\nu}\varepsilon_a = \frac{E}{1-\nu}\frac{a - a_0}{a_0}, \tag{3}$$

where ε_a is the in-plane strain and a_0 is the unstrained reference, with a value of 3.111 31 Å.[46] Young's modulus and Poisson's ratio used were 257 GPa and 0.203,[47] respectively.

The different methods used for stress evaluation are not in agreement with each other. The biaxial stress given by wafer curvature and FTIR measurements is tensile for all films in as-deposited and annealed states. In-plane XRD gives the residual stress as tensile as well for AlN on Al (I). The HRXRD measurements result in compressive stress for all AlN on Al (II) films. For AlN on Si (I), the HRXRD results show that the stress turns from compressive to tensile after annealing at 800 °C. It seems that the films are not in a state of pure biaxial residual stress and that triaxial strains are present as well. A likely source for the apparent triaxial strain are the impurity atoms observed with FTIR and they are known to be incorporated into ALD films.[14,15] Moreover, the ALA step might incorporate Ar atoms into the film in addition to the incorporation of various hydrocarbons from the ALD precursor by-products, N from the NH_3 plasma, and O from the residual gasses in the ALD reactor. Especially, O impurities can increase the lattice constant *c*, resulting in apparent biaxial compressive stress, by substituting N^{3-} with O^{2-} and creating Al vacancies.[48] The higher measured GPC of 1.2 Å compared to previously reported 0.9 Å (Ref. 17) is likely caused by the incorporation of impurity atoms as well.

Surprisingly, according to the wafer curvature measurements, the residual stress of the AlN on Al deposited at 300 °C seems to be nearly as high as the residual stress of MOCVD AlN grown at 1125 °C [1.53 (Ref. 8) and 3.19 GPa (Ref. 13)]. Clearly, the thermomechanical stresses, due to the deposition temperature and CTE mismatch between AlN and the substrate, are not the dominating source of residual stresses. Furthermore, good AlN crystal quality seems to lead to high residual stresses, which has been observed previously as well.[49]

The A_1(TO) line of the as-deposited and annealed films is at a higher wavenumber than what is generally reported for AlN [612 cm^{-1} (Refs. 44 and 50)] and this corresponds to tensile stress. Postdeposition annealing decreases the wavenumber, reaching a minimum after annealing at 600 °C, which would then correspond to a decrease in the residual stress. The estimated stress is significantly higher than using other methods. This is at least in part explained by the lack of *c*-axis orientation, which decreases the in-plane Young's modulus of AlN because the lattice is softer in the *c*-axis direction than in the *a*-axis. On the other hand, the decrease in the E_1(TO) wavenumber indicates that the biaxial residual stress increases with the annealing temperature[43] and reaches a maximum at 800 °C.

TABLE IV. 0002 HRXRD results of AlN on Si (I) and Al (II) after annealing.

Temp.	AlN on Si (I)			AlN on Al (II)				
(°C)	2θ (deg)	FWHM (deg)	*c* (Å)	2θ (deg)	FWHM (deg)	*c* (Å)	ω (deg)	FWHM (deg)
As-dep.	35.94	0.49	4.99	35.94	0.42	4.99	17.56	6.58
300	35.94	0.51	4.99	35.92	0.46	5.00	17.61	6.87
400	35.96	0.50	4.99	35.93	0.43	4.99	17.66	6.41
600	36.03	0.50	4.98	35.91	0.45	5.00	17.09	9.72
800	36.18	0.52	4.96					
1000	36.12	0.55	4.97					

The in-plane strain measured using in-plane XRD does not seem to change between the as-deposited film and film annealed at 1000 °C for 10 h (−0.08% and −0.07%). However, after annealing at 800 °C, the measured in-plane strain is 0.17%, which corresponds to a biaxial residual stress of 0.54 GPa.

The calculated residual stress contains significant uncertainty from the selection of Young's modulus, Poisson's ratio, and unstrained reference lattice constants[45] and FTIR line locations. Moreover, the crystallinity of AlN affects its Young's modulus[8] and can range from 257 to 346 GPa for a low-crystallinity ALD film and a high-crystallinity MOCVD film, respectively. Preliminary bulge testing of ALA ALD AlN thin films shows that Young's modulus might be even significantly lower than 257 GPa. However, more testing is required to confirm this.

Table IV summarizes the HRXRD results of AlN on Si and Al after annealing. See supplementary material[54] for the 2θ–ω diffractograms and XRCs about the AlN0002 on Al. Even though annealing results in a reduction of impurities, it does not seem to improve the crystal quality of AlN on Si. On the contrary, the FWHM of the AlN0002 reflection increases from 0.49° to 0.55° when annealed at 1000 °C, which indicates that the crystallite size becomes smaller. At the same time, the lattice constant *c* decreases from 4.99 to 4.97 Å as annealing reduces the number of impurities and the triaxial stress state turns into mostly biaxial.

The observed decrease in the width of the E_1(TO) line as a result of postdeposition annealing is likely due to the relaxation of residual stresses[44] since the XRD results show that the crystal quality did not increase. Moreover, annealing seems to cause crystallization of randomly oriented grains, which is seen as the slight increase of the A_1(TO) line intensity and as the emergence of the 10*i*1 reflection in in-plane XRD.

Even though annealing after deposition did not improve the crystal quality of AlN on Si directly, it might improve the piezoelectric properties of AlN, because oxygen impurities can generate several electrically active defects and thus reduce the piezoelectric properties.[51] Oxygen content is also detrimental to the crystal quality[52] and resistivity[48] of AlN. Moreover, the oxygen impurities are a possible cause for the low dielectric strength observed in piezoelectric testing. The effect of carbon impurities on the piezoelectric properties and crystal quality of AlN has not been studied. However, they might change the carrier concentration in AlN and affect the electrical resistivity.[53] Despite the impurities, the measured resistivity of AlN on Si was high.

On Al, annealing at 400 °C seems to improve the crystal quality and preferential orientation of AlN, which is seen as a considerable increase in the intensity of the AlN0002 XRC. However, the crystal quality could not be further improved by increasing the annealing temperature because of the developed fractures. Annealing does not seem to significantly change the stress state of the AlN film on Al based on the HRXRD results. Based on the FTIR and XRD results of AlN on Si, an annealing temperature of 800 °C is required to reduce the number of impurities in the film and this could not of course be reached on AlN on Al. The grain size or the surface morphology of the AlN film on Si or Al is not affected by annealing, according to AFM.

In-plane XRD does not show any significant changes to the lattice constant *a* of AlN on Al or the widths of the 10*i*0 or 11*i*0 reflections as a result of postdeposition annealing. However, the intensity of especially the 10*i*0 reflection seems to increase. Moreover, annealing seems to cause recrystallization in AlN on Si. A small peak is detected in the in-plane XRD $2\theta_\chi$–ϕ diffractograms around 37.7°, which corresponds to the AlN10*i*1, after annealing at temperatures of 800 and 1000 °C.

IV. CONCLUSIONS

Aluminum nitride thin films were grown using plasma-enhanced atomic layer deposition with *in situ* Ar plasma annealing on bare Si, and Al and Pt metalized substrates. The microstructure and crystal quality of the AlN films were characterized using XRD and TEM. The films were further studied using AFM, FTIR, and spectroscopic ellipsometry. In addition to the substrate curvature measurements, the mechanical stresses were estimated from the XRD and FTIR measurements. The conformal coverage of the plasma ALD process was evaluated by depositing AlN on vertical sidewalls and measuring the film thickness.

Even though previous experiments show that the crystal quality of AlN can be improved using *in situ* plasma annealing compared to conventional thermal or plasma-enhanced ALD,[17,18] the results presented here show that the underlying layer on which AlN is deposited needs to be carefully selected to enhance the crystal quality. In addition to a matching in-plane lattice constant, the underlying layer needs to have a high preferential orientation. Despite the improvement in the crystal quality, all the films still contained randomly oriented grains in addition to the preferentially (0002) oriented grains. The best crystal quality was reached when AlN was deposited on the Al layer with (111) texture. In addition to preferential (0002) orientation, the AlN layer was in-plane oriented with the orientational relationship AlN(0002)||Al(111) AlN[11*i*0]||Al[110]. The AlN layers on Si or Al and Pt without preferential orientation did not have a mosaic structure and were only weakly (0002) oriented. The conformal coverage on vertical sidewalls of the process is excellent for in-plane actuation and sensing.

The residual biaxial stresses given by the substrate curvature measurements are 1.56 GPa for the AlN film with mosaic texture on Al and only 0.42 GPa for AlN on Si. The biaxial stresses given by the lattice constant *c*, on the other hand, are −1.68 and −1.62 GPa for AlN on Al and Si, respectively. The most likely explanation for the discrepancy between the results is the incorporation of impurities, especially oxygen, which causes the expansion of the AlN crystal structure in the direction of the *c*-axis. In addition to oxygen, the films contained hydrocarbon and nitrogen impurities.

Annealing the films under vacuum after deposition starts to decrease the number of impurities at a temperature of 800 °C by eliminating Al-N_2 complexes and at 1000 °C hydrocarbon and oxygen are removed as well. Annealing and reduction of impurities does not improve the crystal quality of AlN and annealing recrystallized AlN into randomly oriented grains. The crystal quality of AlN on Al improved when annealed at 400 °C. However, annealing at higher temperatures fractured AlN on Al. The residual stresses are most likely relaxed during annealing, but the complex stress state of the films makes this somewhat unclear. No other changes were observed as a result of annealing.

ACKNOWLEDGMENTS

Österlund appreciates funding from the European Space Agency (NPI Grant No. 4000116390) and Aalto ELEC Doctoral School. Seppänen acknowledges support from the Walter Ahlström foundation. Glenn Ross is acknowledged for his help with FIB and TEM. Okmetic Oy is acknowledged for providing the silicon wafers. This research was performed at the Aalto University OtaNano—Micronova Nanofabrication Centre and Nanomicroscopy Center.

DATA AVAILABILITY

The data that support the findings of this study are available from the corresponding author upon reasonable request.

REFERENCES

[1] G. Wingqvist, Surf. Coat. Technol. **205**, 1279 (2010), iCMCTF 2010 Special Issue.

[2] T. Y. Lee and J. T. Song, Thin Solid Films **518**, 6630 (2010).

[3] M. D. Williams, B. A. Griffin, T. N. Reagan, J. R. Underbrink, and M. Sheplak, J. Microelectromech. Syst **21**, 270 (2012).

[4] S. Akhbari, F. Sammoura, S. Shelton, C. Yang, D. Horsley, and L. Lin, "Highly responsive curved aluminum nitride pMUT," in *Proceedings of IEEE 27th International Conference on Micro Electro Mechanical Systems (MEMS)* (IEEE, San Francisco, 2014), pp. 124–127.

[5] D. Gong, H. Cai, Y. Xia, S. Ma, H. Liu, Y. Chiu, and Y. Jin, "Fabrication and characterization of AlN based piezoelectric micromachined ultrasonic transducer for contact sensing," in *Proceedings of 19th International Conference on Electronic Packaging Technology (ICEPT)* (IEEE, Shanghai, 2018), pp. 1442–1447.

[6] S. Trolier-McKinstry and P. Muralt, J. Electroceram. **12**, 7 (2004).

[7] M.-A. Dubois and P. Muralt, Sens. Actuators, A **77**, 106 (1999).

[8] E. Österlund, J. Kinnunen, V. Rontu, A. Torkkeli, and M. Paulasto-Kröckel, J. Alloys Compd. **772**, 306 (2019).

[9] D. Zhuang and J. Edgar, Mater. Sci. Eng. R Rep. **48**, 1 (2005).

[10] M. Ramezani, V. Felmetsger, N. Rudawski, and R. Tabrizian, IEEE Trans. Ultrason., Ferroelectr., Freq. Control **68**, 753–759 (2020).

[11] H. Cui, R. Hensleigh, D. Yao, D. Maurya, P. Kumar, M. G. Kang, S. Priya, and X. R. Zheng, Nat. Mater. **18**, 234 (2019).

[12] A. Yanguas-Gil, Y. Yang, N. Kumar, and J. R. Abelson, J. Vac. Sci. Technol. A **27**, 1235 (2009).

[13] E. Österlund, S. Suihkonen, G. Ross, A. Torkkeli, H. Kuisma, and M. Paulasto-Kröckel, J. Cryst. Growth **531**, 125345 (2020).

[14] N. Nepal, S. Qadri, J. Hite, N. Mahadik, M. Mastro, and C. Eddy, Jr., Appl. Phys. Lett. **103**, 082110 (2013).

[15] M. Broas, P. Sippola, T. Sajavaara, V. Vuorinen, A. Pyymaki Perros, H. Lipsanen, and M. Paulasto-Kröckel, J. Vac. Sci. Technol. A **34**, 041506 (2016).

[16] T. Nguyen, N. Adjeroud, S. Glinsek, Y. Fleming, J. Guillot, P. Grysan, and J. Polesel-Maris, APL Mater. **8**, 071101 (2020).

[17] H.-Y. Shih, W.-H. Lee, W.-C. Kao, Y.-C. Chuang, R.-M. Lin, H.-C. Lin, M. Shiojiri, and M.-J. Chen, Sci. Rep. **7**, 1 (2017).

[18] H. Seppänen, I. Kim, J. Etula, E. Ubyivovk, A. Bouravleuv, and H. Lipsanen, Materials **12**, 406 (2019).

[19] M. Bosund, T. Sajavaara, M. Laitinen, T. Huhtio, M. Putkonen, V.-M. Airaksinen, and H. Lipsanen, Appl. Surf. Sci. **257**, 7827 (2011).

[20] S. Kobayashi, Rigaku J. **26**(1), 3–11 (2010).

[21] A. Mazzalai, D. Balma, N. Chidambaram, L. Jin, and P. Muralt, "Simultaneous piezoelectric and ferroelectric characterization of thin films for MEMS actuators," in *Proceedings of 2013 Joint IEEE International Symposium on Applications of Ferroelectric and Workshop on Piezoresponse Force Microscopy* (IEEE, Prague, 2013), pp. 363–366.

[22] J. Borges, F. Vaz, and L. Marques, Appl. Surf. Sci. **257**, 1478 (2010).

[23] Z.-Y. Wang, *et al.*, Nanoscale Res. Lett. **10**, 46 (2015).

[24] A. Artieda, M. Barbieri, C. S. Sandu, and P. Muralt, J. Appl. Phys. **105**, 024504 (2009).

[25] W. Wang, W. Yang, Z. Liu, Y. Lin, S. Zhou, H. Qian, F. Gao, and G. Li, CrystEngComm **16**, 4100 (2014).

[26] C. Sun, P. Kung, A. Saxler, H. Ohsato, K. Haritos, and M. Razeghi, J. Appl. Phys. **75**, 3964 (1994).

[27] H. Loebl, C. Metzmacher, R. Milsom, P. Lok, F. Van Straten, and A. Tuinhout, J. Electroceram. **12**, 109 (2004).

[28] S.-H. Lee, J.-K. Lee, and K. H. Yoon, J. Vac. Sci. Technol., A **21**, 1 (2003).

[29] R. S. Naik, *et al.*, IEEE Trans. Ultrason., Ferroelectr., Freq. Control **47**, 292 (2000).

[30] J. Bjurström, D. Rosén, I. Katardjiev, V. M. Yanchev, and I. Petrov, IEEE Trans. Ultrason., Ferroelectr., Freq. Control **51**, 1347 (2004).

[31] F. Martin, P. Muralt, M.-A. Dubois, and A. Pezous, J. Vac. Sci. Technol., A **22**, 361 (2004).

[32] K. Tonisch, V. Cimalla, C. Foerster, D. Dontsov, and O. Ambacher, Phys. Status Solidi C **3**, 2274 (2006).

[33] H. Demiryont, L. Thompson, and G. Collins, J. Appl. Phys. **59**, 3235 (1986).

[34] M. L. Panchula and J. Y. Ying, J. Am. Ceram. Soc. **86**, 1114 (2003).

[35] J. Coates, "Interpretation of infrared spectra, a practical approach," in *Encyclopedia of Analytical Chemistry: Applications, Theory and Instrumentation* (John Wiley & Sons, Hoboken, 2006).

[36] A. P. Perros, H. Hakola, T. Sajavaara, T. Huhtio, and H. Lipsanen, J. Phys. D: Appl. Phys. **46**, 505502 (2013).

[37] U. Mazur and A. C. Cleary, J. Phys. Chem. **94**, 189 (1990).

[38] X. D. Wang, K. Hipps, and U. Mazur, Langmuir **8**, 1347 (1992).

[39] D. N. Goldstein, J. A. McCormick, and S. M. George, J. Phys. Chem. C **112**, 19530 (2008).

[40] R. Dalmau, R. Collazo, S. Mita, and Z. Sitar, J. Electron. Mater. **36**, 414 (2007).

[41] A. Perros, M. Bosund, T. Sajavaara, M. Laitinen, L. Sainiemi, T. Huhtio, and H. Lipsanen, J. Vac. Sci. Technol., A **30**, 011504 (2012).

[42] P. Sippola, *et al.*, J. Vac. Sci. Technol., A **36**, 051508 (2018).

[43] J. Edgar, C. Carosella, C. Eddy, and D. Smith, J. Mater. Sci.: Mater. Electron. **7**, 247 (1996).

[44] A. Sanz-Hervás, E. Iborra, M. Clement, J. Sangrador, and M. Aguilar, Diamond Relat. Mater. **12**, 1186 (2003).

[45] M. Moram and M. Vickers, Rep. Prog. Phys. **72**, 036502 (2009).

[46] D. Nilsson, E. Janzén, and A. Kakanakova-Georgieva, J. Phys. D: Appl. Phys. **49**, 175108 (2016).

[47] A. Wright, J. Appl. Phys. **82**, 2833 (1997).

[48] M. Signore, A. Taurino, D. Valerini, A. Rizzo, I. Farella, M. Catalano, F. Quaranta, and P. Siciliano, J. Alloys Compd. **649**, 1267 (2015).

[49] S. Raghavan and J. M. Redwing, J. Cryst. Growth **261**, 294 (2004).

[50] L. Vergara, J. Olivares, E. Iborra, M. Clement, A. Sanz-Hervás, and J. Sangrador, Thin Solid Films **515**, 1814 (2006).

[51] L. Vergara, M. Clement, E. Iborra, A. Sanz-Hervás, J. G. López, Y. Morilla, J. Sangrador, and M. Respaldiza, Diamond Relat. Mater. **13**, 839 (2004).

[52] V. Brien and P. Pigeat, J. Cryst. Growth **310**, 3890 (2008).

[53] P. Bogusławski and J. Bernholc, Phys. Rev. B **56**, 9496 (1997).

[54] See supplementary material at https://doi.org/10.1116/6.0000724 for AFM and XRD results.